


Article

Response of a Cold-Electron Bolometer on THz Radiation from a Long $\text{YBa}_2\text{Cu}_3\text{O}_{7-\delta}$ Bicrystal Josephson Junction

Leonid Revin ^{1,2}, Andrey Pankratov ^{1,2,3,*} , Anna Gordeeva ^{1,2}, Dmitry Masterov ¹, Alexey Parafin ¹, Viktor Zbrozhek ² and Leonid Kuzmin ^{2,4}

¹ Institute for Physics of Microstructures of RAS, GSP-105, Nizhny Novgorod 603950, Russia; rls@ipmras.ru (L.R.); a.gordeeva@nntu.ru (A.G.); masterov@ipmras.ru (D.M.); parafin@ipmras.ru (A.P.)

² Laboratory of Superconducting Nanoelectronics, Nizhny Novgorod State Technical University, Nizhny Novgorod 603950, Russia; viktorphoenix@mail.ru (V.Z.); kuzmin@chalmers.se (L.K.)

³ Institute of Information Technology, Mathematics and Mechanics (IITMM), Lobachevsky State University of Nizhny Novgorod, Nizhny Novgorod 603950, Russia

⁴ Department of Microtechnology and Nanoscience, Chalmers University of Technology, SE-41296 Gothenburg, Sweden

* Correspondence: alp@ipmras.ru

Received: 4 October 2020; Accepted: 23 October 2020; Published: 29 October 2020



Abstract: The response of the Cold-Electron Bolometers (CEBs), integrated into a 2-D array of dipole antennas, has been measured by irradiation from $\text{YBa}_2\text{Cu}_3\text{O}_{7-\delta}$ (YBCO) 50 μm long Josephson junction into the THz region at frequencies from 0.1 to 0.8 THz. The possibility of controlling the amplitude-frequency characteristic is demonstrated by the external magnetic field in the traveling wave regime of a long Josephson junction. The YBCO junction has been formed on the bicrystal $\text{Zr}_{1-x}\text{Y}_x\text{O}_2$ (YSZ) substrate by magnetron sputtering and etching of the film. CEBs have been fabricated using an Al multilayer structure by a self-aligned shadow evaporation technique on Si substrate. Both receiver and oscillator have been located inside the same cryostat at 0.3 K and 2.7 K plates, respectively.

Keywords: anisotropic high- T_c grain-boundary; YBCO Josephson oscillator; cold-electron bolometer; sine-Gordon equation

1. Introduction

The high precision measurements of the polarization in the cosmic microwave background (CMB) radiation is one of the major tasks in modern cosmology, needed to detect primordial B-modes. B-mode is a curl component of the polarization of CMB, which, as believed, left by the primordial gravitational waves during the inflation stage of the universe's evolution. Predicted by theory, if detected, it is assumed to be a sufficient evidence of the inflationary epoch in the early universe [1].

The development of multichroic focal planes for measurements of the CMB is important for increasing the sensitivity of an experiment as well as for removing the contamination due to galactic foregrounds, which is becoming the limiting factor in CMB measurements [2]. The cold-electron bolometer (CEB) is an attractive candidate for these measurements because the decoupling of the phonon and electron subsystems in the tiny absorber gives it such advantages as high sensitivity and high saturation power [3,4] as well as the immunity to cosmic rays [5]. CEBs can be used for on-chip LC-filtering due to a series resonance of the SIN junction capacitance and the kinetic inductance of the NbN strip [6–8] or the reactance of slot antennas connected by coplanar lines [9,10]. This property is used for the creation of multichroic pixels with CEBs.

The most actual task for the elaboration of multichroic bolometric systems is developing of the broadband radiation source with narrow spectral linewidth, placed inside a cryostat to avoid multiple reflections and sensitivity loss due to open windows. In recent years frequency calibrations of CEBs have been carried out using external sources of the THz range [11,12] or filtered broadband thermal sources [13,14]. These solutions are not very suitable when repetitive calibrations in a wide range of frequencies for different resonant structures are required. Here we look at a calibration source based on the long YBCO Josephson junction (JJ), having a continuous frequency tuning in a wide frequency range from 0.1 to 2 THz.

High critical temperature bicrystal Josephson junctions can be used for THz frequency band oscillators, detectors and Hilbert spectrometers, as was shown, for example, in [15,16]. Even relatively weak radiation of a long YBCO JJ can be useful for spectral calibration of highly sensitive cryogenic detectors. Josephson generators are one of the most convenient sources of GHz and subTHz signals [17] because they have the potential to generate in a wide frequency range, and their main frequency is easily determined by the Josephson relation. Measurements of high-temperature JJs, both $\text{YBa}_2\text{Cu}_3\text{O}_{7-\delta}$ and $\text{Bi}_2\text{Sr}_2\text{CaCu}_2\text{O}_8$, require the use of very sensitive detectors, such as integrated superconducting heterodyne receivers [18–20], bolometers [21,22], quantum-dot single-photon detectors [23]. For the analysis of planar YBCO junctions in all works short junctions were used [15–17]. In this work, we analyze the regime that occurs only in a long JJ under the effect of the magnetic field, called a “traveling wave” or “flux-flow” regime. The study of the flux-flow regime arising in JJ is a subject of practical interest. In a long JJ (length, $L \gg \lambda_J$, where λ_J is the Josephson penetration depth), placed in an external magnetic field, the fluxons can be created at one edge of the junction and after movement along the junction radiated at the opposite edge, creating the so-called fluxon motion mode. When the fluxon velocity u becomes close to the EM wave phase velocity \bar{c} , a current step (velocity-matching or flux-flow step) appears at the current-voltage (IV) characteristic. While for low- T_c Josephson junctions this regime was investigated both experimentally [24–31] and theoretically [32–44], there were just a few works for high- T_c JJs in this regime [45–48], and their analysis was limited to the study of dc characteristics.

This work aims to study theoretically and experimentally the flux-flow regime and THz radiation, arising in this regime, of long YBCO bicrystal Josephson junction (YBCO FFO), by means of the CEB receiver.

2. Experimental Setup

CEB represents SINIS (SIN—superconductor-insulator-normal metal) junctions $\text{Al}/\text{Al}_2\text{O}_3/\text{Al-Fe}/\text{Al}_2\text{O}_3/\text{Al}$ with a normal metal tiny nanoabsorber made of aluminum with suppressed superconductivity due to underlayer of Fe. The saturation power for one CEB is about 0.5 pW. Taking into account the expected power load, the 2-dimensional array of CEBs [49] has been realized as a meander-type structure [3,12]. The receiving system represents a single pixel for the Olimpo balloon experiment, optimized for power loads up to 100 pW. The unit cell of dipoles is a modification of the dense rectangular grid, distributed in a more sparse way over the unit cell [49]. The serial and parallel DC connections of CEBs are optimized for impedance matching and minimal overall system noise [3]. The pairs of $\lambda/2$ dipoles sensitive to both orthogonal linear polarizations are connected to each other by dc lines with 1 μm width. The impedance of each bolometer comes from a series connection of a 30 Ohm resistance and a 55 fF capacitance. In difference with the original design [3,12], the unetched 280 μm substrate has been used to match the bolometer bandwidth with the YBCO oscillator antenna bandwidth in the range 240–280 GHz.

The long grain boundary Josephson junctions (GBJs) were fabricated by on-axis dc magnetron sputtering [50] of $\text{YBa}_2\text{Cu}_3\text{O}_{7-\delta}$ thin films on the surface of $24^\circ[001]$ -tilt $\text{Zr}_{1-x}\text{Y}_x\text{O}_2$ bicrystal substrates and further etching. The length of the junctions L along the grain boundary (sample photo in Figure 1) was 50 μm , the thickness was 0.3 μm . We have obtained critical current density 370 kA/cm^2 and the $I_c R_n$ product of 1.54 mV for $T = 6$ K. The junctions were very long since their lengths are

much larger than the Josephson penetration depth $\lambda_J = \sqrt{\Phi_0 / (2\pi\mu_0 J_c d)} = 0.6 - 0.9 \mu\text{m}$ ($T \sim 6 \text{ K}$), which determines the size of a fluxon in the junction. Based on the analysis of the transport properties, the best structures were selected and located at the center of the Si lens for effective radiation. The perpendicular to the grain boundary magnetic field B_e of the order of tenths Gauss was produced by a copper wire coil with many adjacent loops (solenoid). The coil inner diameter of 10 mm was at least one order of magnitude larger than the junction length. Therefore, the magnetic field in the vicinity of the junction was assumed to be nearly uniform [50]. We have checked that the detector itself has no response to the magnetic field through the Josephson oscillator coil.

In Figure 1 the scheme of the experimental setup is presented. The distance between the detector (CEBs) and the source (YBCO) is 3 cm. The YSZ substrate with the YBCO GBJ was attached to the Si hyperhemisphere lens with 4 mm diameter at the 2.7 K plate of 3He refrigerator. The radiation from YBCO goes after the lens through the copper horn to the Si substrate with the CEBs from the bottom side. The receiving detector consists of an array of 192 CEBs, connected in 4 parallel rows to match with JFET amplifier impedance [3]. The array is surrounded by a copper shield [14] to avoid radiation from other directions and is attached to the 0.3 K cryostat plate.

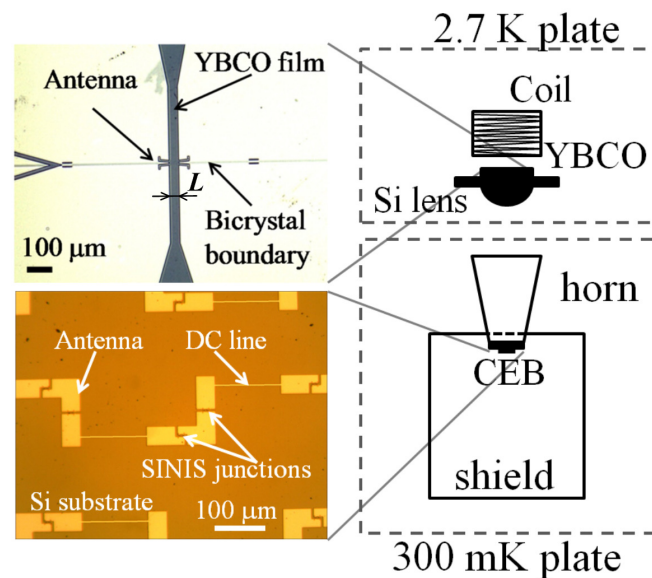


Figure 1. The view of the experimental setup, its schematic representation and samples design.

3. Experimental Results

In Figure 2, the current-voltage characteristics of CEBs are shown for the case of no signal (no bias of YBCO oscillator) and the case under YBCO JJ power load. Bolometer response is defined as a voltage difference at a fixed bias current through the CEBs array with and without the JJ radiation. Based on the response characteristic (the inset of Figure 2) the bias current for the bolometer has been chosen aside from the maximum response since there is a minimal value of noise-equivalent-power [3].

Changing the current through the Josephson junction (for zero current through the coil, creating the magnetic field), the signal from the bolometer and the voltage on the YBCO oscillator (which is connected with the oscillation frequency via the Josephson relation) have been measured, see Figure 3. The detected signal consists of two components. The first one, smooth, corresponds to infrared radiation from an overheated Josephson junction and magnetic coil. It can be well described by a spline line $V_{CEB} = aV_{YBCO}^2 + bV_{YBCO} + c$ (dashed curve in Figure 3). The second component, uneven, is a generation signal at the Josephson frequency $f = 2eV_{YBCO}/h$ and is sensitive to a magnetic field. To reduce the first component, the measurements were carried out as quickly as possible, which was allowed without loss of accuracy thanks to the fast response of CEBs. The adjustment of JJ bias and

measurement time of the bolometer response to the JJ radiation of a given frequency is milliseconds, while the duration of the thermal response due to system overheating is seconds.

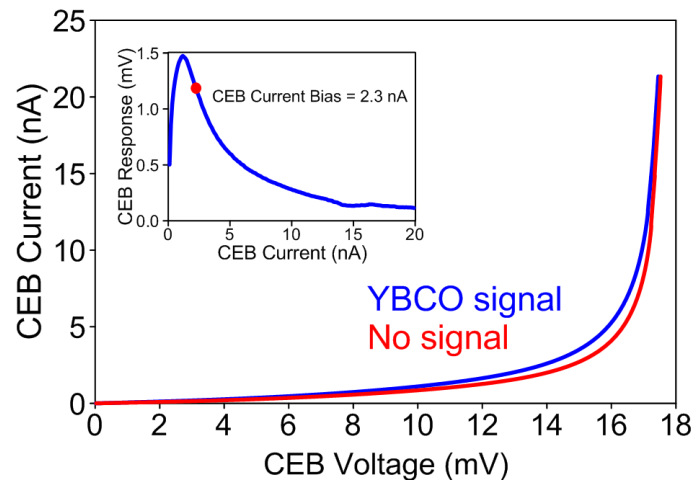


Figure 2. Current-voltage characteristic of bolometer for the case of no signal and under the YBCO JJ radiation. The inset: CEBs response as a function of bias current. The mark corresponds to the used bias.

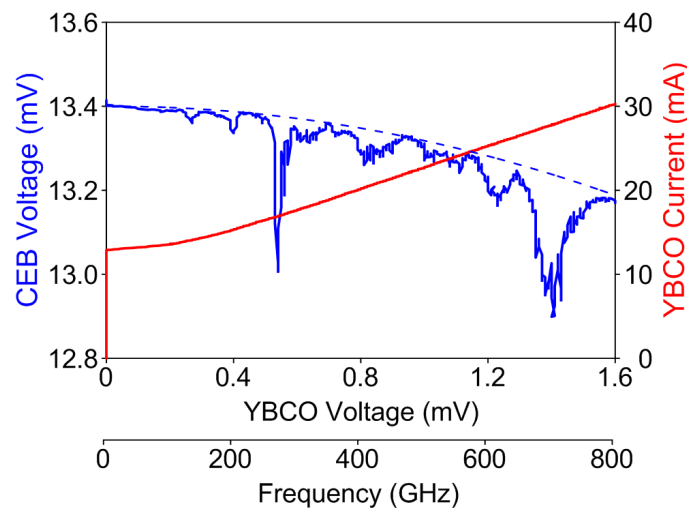


Figure 3. Left: CEBs voltage (solid curve) and a fitting spline (dashed curve). Right: current-voltage characteristic of YBCO oscillator.

Subtracting the component of the background heating signal, the response of the bolometer to the YBCO JJ radiation as a function of frequency was obtained (blue solid curve in Figure 4, marked as YBCO, for the case of zero magnetic field when the only bias current through JJ was varied). It is seen that the response consists of several peaks with different heights. Comparing it with the CEBs amplitude-frequency characteristic (AFC) obtained by the calibrated backward-wave oscillator (BWO) source (green symbols in Figure 4), one can conclude that the peak positions are determined both by characteristics of the receiving and the radiating systems. If in addition to bias current, one starts to vary the magnetic field (current through the coil), the response grows significantly and larger peaks can be visible (red dashed curve in Figure 4). It should be noted that the CEB AFC measurements were performed with BWO source placed outside the cryostat, and the signal was strongly attenuated both by attenuators placed at BWO, and also by null-density filters at the cryostat windows to prevent from 0.3 K plate overheating due to incoming THz signal. The internal inhomogeneity of the BWO amplitude–frequency characteristic was properly taken into account when plotting the corresponding curve of Figure 4.

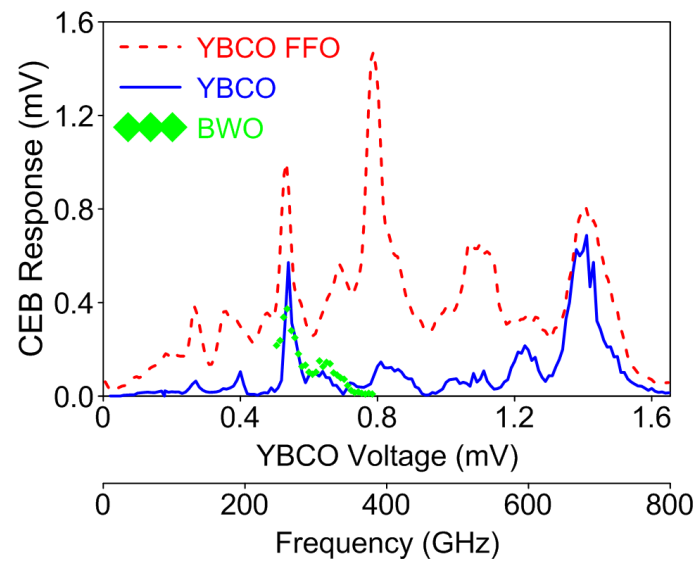


Figure 4. CEBs response depending on YBCO voltage (oscillation frequency). Comparison of the CEBs signal from BWO and YBCO sources. Signatures of YBCO and YBCO FFO correspond to the case of zero magnetic field and case of magnetic field variation.

Figure 5 presents the experimental IV curves of YBCO JJ for various values of the applied magnetic field. The color indicates the level of CEBs response. We observe field dependent steps, characteristic to the travelling wave regime in a long Josephson junction. It should be noted that in difference with Nb junctions [38], for YBCO structures, due to larger damping, it is rather difficult to distinguish between various step types, such as displaced linear slopes, Fiske steps and velocity matching (VM) steps [51,52]. The separate peaks, repeated at the same frequency for all magnetic fields, are attributed to overlapping responses between different harmonics of antennas of YBCO oscillator and CEBs array. The AFC of the YBCO antenna has recently been measured in [52] from the height of Shapiro step in the frequency range from 240 to 350 GHz with the same BWO as a radiation source. The maximum response has been observed from 250 to 280 GHz, which corresponds to the first harmonics of the YBCO JJ dipole antenna.

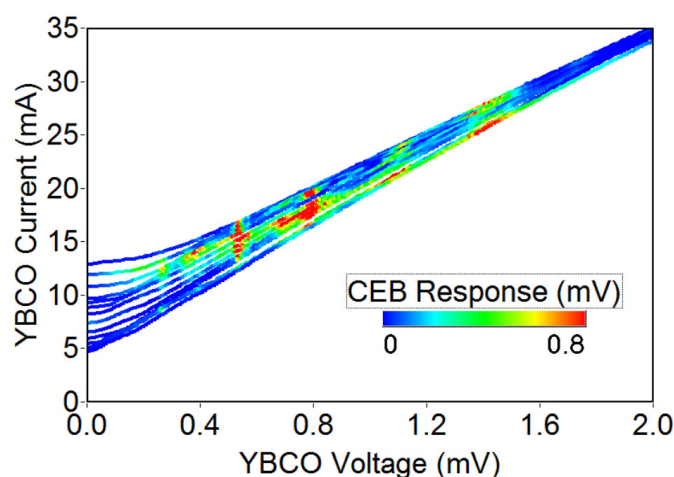


Figure 5. The experimental IV curves of bicrystal junction $L = 50 \mu\text{m}$ correspond to the increasing magnetic field (from top to bottom). The color indicates the level of CEBs response.

Figure 6 shows the CEBs response (dependent on the absorbed power) for several values of the external magnetic field. For convenience, the curves starting from the second one are shifted up by

0.5 mV relative to the previous one. To characterize this picture, let us smooth out the dependences (grey dashed curves in Figure 6) and find the voltage of the local maximum of the response V_{mr} and the value of response S_{mr} . It can be seen that for larger magnetic fields, the position of maxima is shifted towards higher voltages as it must in the traveling wave regime, see also Figure 5.

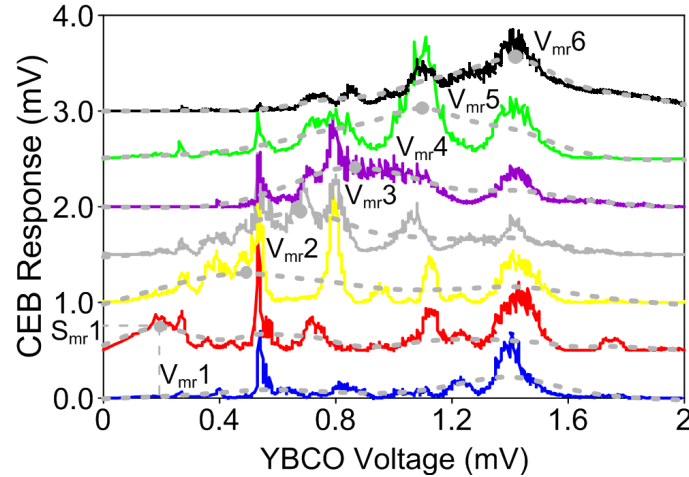


Figure 6. CEBs response for increasing magnetic fields through the YBCO oscillator. For convenience, the curves starting from the second one are shifted up by 0.5 mV relative to the previous one. Marks correspond to the local maximum of each smoothed characteristic.

An array of fluxons, which for a high magnetic fields transforms into the travelling wave, propagates along the junction with the phase velocity $u = V_{dc} / (d\mu_0 H_e)$ [46], where V_{dc} is the average voltage across the junction, H_e is the external magnetic field applied in the direction perpendicular to the grain boundary, d is the effective magnetic thickness of the barrier and μ_0 is the magnetic constant. The voltage at the top of the flux-flow step on the IV characteristic is determined by the VM condition: the velocity u approaches the Swihart velocity \bar{c} and, hence, $V_{vm} \approx \bar{c}d\mu_0 H_e = \bar{c}dB_e$. This ratio is confirmed experimentally: the voltage position of the step for larger fields depends linearly on the applied field [46,51]. The voltage range from 0.2 to 1.1 mV corresponds to Josephson frequencies ranging from about 100 to 550 GHz. The VM step becomes smaller and wider as the voltage is increased. This is expected from the increasing surface losses at higher frequencies [38]. The same picture is observed for the received power (CEBs response): the applied magnetic field allows to increase the response voltage V_{mr} in a wider frequency range.

To find out what the maximum power is possible for a given voltage (frequency) in the travelling wave regime, it is necessary to investigate the $S_{mr}(V_{mr})$ characteristic (red dashed curve in Figure 7), i.e., the envelope of the maximums of each of smoothed curves from Figure 6. Each point corresponds to a different magnetic field value. The dependence of the CEBs response on the YBCO voltage $S_{mr}(V_{mr})$ has a flat maximum at the frequency range ~ 350 – 500 GHz. The form of this curve also depends on surface losses, the antenna system, impedance matching, etc. It is interesting to compare the power from the JJ, operating in the phase rotation regime, when the external magnetic field is zero and the frequency is tuned by the bias current variation only (blue solid curve in Figure 7), and YBCO FFO, operating in the traveling wave regime with the frequency tuned by both bias current and magnetic field variation. One can see that in the latter case the oscillation power increases and can be observed in a much wider frequency range. Therefore, this experimental result is a confirmation of recent theoretical observation that the oscillation power in the case of lag-synchronization (occurring also in the travelling wave regime) can be several orders of magnitude larger than for perfect in-phase synchronization of chain elements [53]. These results also show the advantages of using long Josephson junctions over short ones to develop an effective THz generator. It should be noted that in the previous work on detecting the generation of a short Josephson junction using a CEB [16], it was shown that

when a magnetic field is applied to the JJ, the amplitude of the received signal decreases, while in our case the amplitude grows.

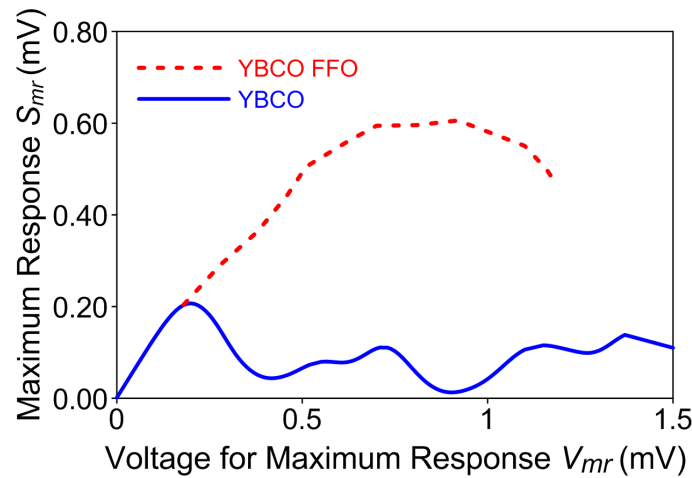


Figure 7. The maximum response depending on YBCO voltage for bicrystal junction with the length $L = 50 \mu\text{m}$ for phase rotation regime (blue solid curve) and traveling wave regime (red dashed curve).

4. Theory

Theoretical analysis is based on the sine-Gordon equation [50,54]:

$$\phi_{tt} + \alpha\phi_t - \phi_{xx} = \beta\phi_{xtt} + \eta - \sin\phi, \quad (1)$$

where indices t and x denote temporal and spatial derivatives, ϕ is the phase order parameter. Space and time are normalized to the Josephson penetration length λ_J and to the inverse plasma frequency ω_p^{-1} , respectively, $\alpha = \omega_p/\omega_c$ is the damping parameter, $\omega_p = \sqrt{2eI_c/\hbar C}$, $\omega_c = 2eI_c R_N/\hbar$, β is the surface loss parameter, η is the bias current normalized to the critical current. The boundary conditions that simulate simple RC-loads, see Refs. [34,38,40,41], have the form:

$$\begin{aligned} \phi(0,t)_x + r_L c_L \phi(0,t)_{xt} - c_L \phi(0,t)_{tt} + \\ \beta r_L c_L \phi(0,t)_{xtt} + \beta \phi(0,t)_{xt} = \Gamma, \end{aligned} \quad (2)$$

$$\begin{aligned} \phi(L,t)_x + r_R c_R \phi(L,t)_{xt} + c_R \phi(L,t)_{tt} + \\ \beta r_R c_R \phi(L,t)_{xtt} + \beta \phi(L,t)_{xt} = \Gamma. \end{aligned} \quad (3)$$

Here $\Gamma = H_e/(\lambda_J J_c)$ is the normalized magnetic field. The dimensionless capacitances and resistances, $c_{L,R}$ and $r_{L,R}$, are the FFO RC-load placed at the left (output) and at the right (input) ends, respectively. The power P of radiation, emitted from the junction output edge is normalized to the Josephson power $P_J = V_J^2/Z_0$, where Z_0 is the characteristic impedance of the junction.

The computer simulations of the sine-Gordon equation are performed for the following parameters: damping $\alpha = 1.5$, surface loss $\beta = 0.1$, and dimensionless junction length $l = 70$.

Figure 8 shows the theoretical IV curves for various values of applied magnetic field Γ . The color indicates the level of radiation power P . In the present case, the antenna bandwidth is not considered, assuming that the junction is perfectly matched to a load in the whole frequency range. We observe the regime of a continuous flow of fluxons, which for larger magnetic fields smoothly transforms into the travelling wave regime. The inset of Figure 8 shows the radiated power level for several values of the magnetic field. Here we marked the voltage position of the maximum power as V_{mp} and the maximum power as P_{mp} .

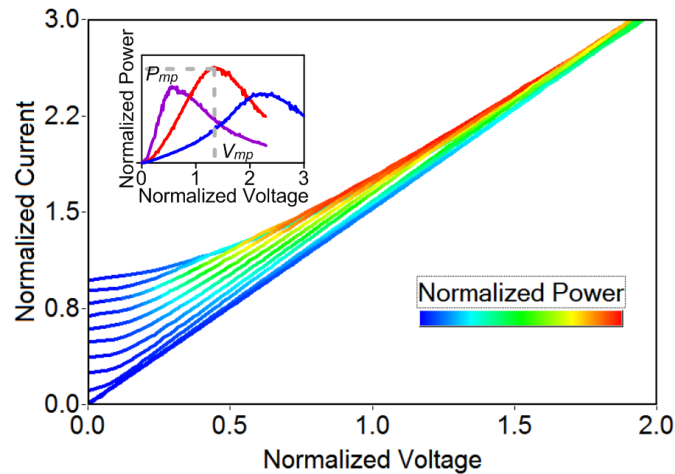


Figure 8. The theoretical IV curves correspond to increasing magnetic field Γ (from top to bottom). The color indicates the level of radiated power. The inset: Power P for various magnetic fields ($\Gamma = 0.6$; 1.6; 2.6) versus normalized voltage.

Figure 9 shows the dependence of the power level versus normalized voltage $P_{mp}(V_{mp})$ for zero external magnetic field (blue solid curve) and nonzero external magnetic field, leading to a traveling wave regime (red dashed curve). Both theoretical curves show the behavior, qualitatively similar to the experiment (see Figure 7), they both have maxima, but the maximum, corresponding to YBCO FFO, is wider and reaches larger values. Therefore, such dependences demonstrate the advantage of a long YBCO JJ, operating in the traveling wave regime, compared with short and long junctions operating in the phase rotation regime, as THz broadband sources.

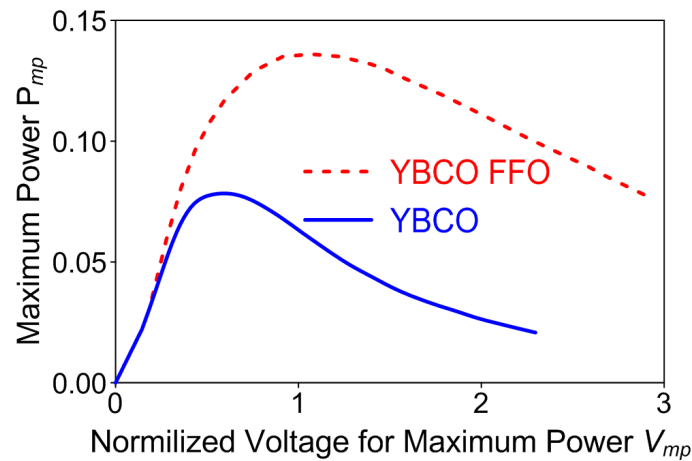


Figure 9. The maximum value of power level depending on voltage for phase rotation regime (blue solid curve) and traveling wave regime (red dashed curve).

5. Conclusions

The investigation of the response of a Cold Electron Bolometer receiver on the THz radiation of long $24^\circ[001]$ -tilt $\text{YBa}_2\text{Cu}_3\text{O}_{7-\delta}$ bicrystal grain-boundary junctions has been performed. The investigation of maximum oscillation power versus magnetic field is performed both experimentally and theoretically and its dependence corresponds to the traveling wave regime. While the antennas of both emitting and receiving systems were tuned in the frequency range from 250 to 320 GHz, the visible response has been detected in windows up to 0.8 THz. The maximal received power as estimated from fitting of CEBs IV response is rather low and of the order of 10 pW, that can be explained by poor matching of YBCO junction with its antenna due to unknown impedance and a difference in the dielectric constant of the JJ

YSZ substrate and Si lens material. Despite the fact that the considered sample of the long YBCO JJ has low generation efficiency, such oscillators can be useful for spectral calibration of low-temperature bolometers, receivers, and single-photon detectors.

Author Contributions: L.R. contributed experiment planning, experiment measurements, data analysis and manuscript preparation. A.P. (Andrey Pankratov) contributed experiment measurements, writing—review and editing. A.G. contributed methodology, experiment planning, manuscript preparation. D.M. contributed research sample preparation. A.P. (Alexey Parafin) contributed research sample preparation. V.Z. contributed experiment planning. L.K. contributed supervision, writing—review and editing. All authors have read and agreed to the published version of the manuscript.

Funding: This research was funded by RSF projects 16-19-10478 (fabrication and investigations of YBCO samples) and 16-19-10468 (fabrication and preliminary calibration of CEB receiver).

Acknowledgments: The authors wish to thank M. Tarasov for help in the CEBs sample fabrication and A. Klushin for help in YBCO film etching.

Conflicts of Interest: The authors declare no conflict of interest. The funders had no role in the design of the study; in the collection, analyses, or interpretation of data; in the writing of the manuscript, or in the decision to publish the results.

References

1. Zmuidzinas, J.; Richards, P.L. Superconducting detectors and mixers for millimeter and submillimeter astrophysics. *Proc. IEEE* **2004**, *92*, 1597. [\[CrossRef\]](#)
2. Cukierman, A.; Lee, A.T.; Raum, C.; Suzuki, A.; Westbrook, B. Hierarchical sinuous-antenna phased array for millimeter wavelengths. *Appl. Phys. Lett.* **2018**, *112*, 132601. [\[CrossRef\]](#)
3. Kuzmin, L.S.; Pankratov, A.L.; Gordeeva, A.V.; Zbrozhek, V.O.; Shamporov, V.A.; Revin, L.S.; Blagodatkin, A.V.; Masi, S.; de Bernardis, P. Photon-noise-limited cold-electron bolometer based on strong electron self-cooling for high-performance cosmology missions. *Commun. Phys.* **2019**, *2*, 104. [\[CrossRef\]](#)
4. Kuzmin, L.S. An array of cold-electron bolometers with SIN tunnel junctions and JFET readout for cosmology instruments. *J. Phys. Conf. Ser.* **2008**, *97*, 012310. [\[CrossRef\]](#)
5. Salatino, M.; de Bernardis, P.; Kuzmin, L.S.; Mahashabde, S.; Masi, S. Sensitivity to Cosmic Rays of Cold Electron Bolometers for Space Applications. *J. Low Temp. Phys.* **2014**, *176*, 323. [\[CrossRef\]](#)
6. Kuzmin, L.S. A Resonant Cold-Electron Bolometer With a Kinetic Inductance Nanofilter. *IEEE Trans. Terahertz Sci. Technol.* **2014**, *4*, 314. [\[CrossRef\]](#)
7. Kuzmin, L.S.; Mukhin, A.S.; Chiginev, A.V. Realization of the Resonant Cold-Electron Bolometer With a Kinetic Inductance Nanofilter for Multichroic Pixels. *IEEE Trans. Appl. Supercond.* **2018**, *28*, 2400304. [\[CrossRef\]](#)
8. Mukhin, A.S.; Kuzmin, L.S.; Chiginev, A.V.; Blagodatkin, A.V.; Zbrozhek, V.O.; Gordeeva, A.V.; Pankratov, A.L. Multifrequency seashell antenna based on resonant cold-electron bolometers with kinetic inductance nanofilters for CMB measurements. *AIP Adv.* **2019**, *9*, 015321. [\[CrossRef\]](#)
9. Kuzmin, L.S.; Blagodatkin, A.V.; Mukhin, A.S.; Pimanov, D.A.; Zbrozhek, V.O.; Gordeeva, A.V.; Pankratov, A.L.; Chiginev, A.V. Multichroic seashell antenna with internal filters by resonant slots and cold-electron bolometers. *Supercond. Sci. Technol.* **2019**, *32*, 035009. [\[CrossRef\]](#)
10. Revin, L.S.; Pimanov, D.A.; Blagodatkin, A.V.; Gordeeva, A.V.; Zbrozhek, V.O.; Masterov, D.V.; Parafin, A.E.; Pavlov, S.A.; Pankratov, A.L.; Rakut, I.V. A Study of a Narrow-Band Receiving System of Cold-Electron Bolometers for the 220 and 240 GHz Channels using an Oscillator Based on the High-Temperature YBCO Superconductor. *Radiophys. Quant. Electron.* **2019**, *62*, 7. [\[CrossRef\]](#)
11. Tarasov, M.A.; Kuzmin, L.S.; Edelman, V.S.; Mahashabde, S.; de Bernardis, P. Optical Response of a Cold-Electron Bolometer Array Integrated in a 345-GHz Cross-Slot Antenna. *IEEE Trans. Appl. Supercond.* **2011**, *21*, 3635. [\[CrossRef\]](#)
12. Matrozova, E.A.; Pankratov, A.L.; Gordeeva, A.V.; Chiginev, A.V.; Kuzmin, L.S. Absorption and cross-talk in a multipixel receiving system with cold-electron bolometers. *Supercond. Sci. Technol.* **2019**, *32*, 084001. [\[CrossRef\]](#)

13. Mukhin, A.S.; Gordeeva, A.V.; Revin, L.S.; Abashin, A.E.; Shishov, A.A.; Pankratov, A.L.; Mahashabde, S.; Kuzmin, L.S. Sensitivity and Noise of Cold-Electron Bolometer Arrays. *Radiophys. Quant. Electron.* **2017**, *59*, 754. [\[CrossRef\]](#)
14. Gordeeva, A.V.; Zbrozhek, V.O.; Pankratov, A.L.; Revin, L.S.; Shamporov, V.A.; Gunbina, A.A.; Kuzmin, L.S. Observation of photon noise by cold-electron bolometers. *Appl. Phys. Lett.* **2017**, *110*, 162603. [\[CrossRef\]](#)
15. Tarasov, M.; Kuzmin, L.; Stepantsov, E.; Kidiyarova-Shevchenko, A. Quasioptical Terahertz Spectrometer Based on a Josephson Oscillator and a Cold Electron Nanobolometer. In *Nanoscale Devices—Fundamentals and Applications, NATO Science Series*; Chapter: Advanced Sensors of Electromagnetic Radiation; Springer: Dordrecht, The Netherlands, 2006; Volume 233.
16. Stepantsov, E.; Tarasov, M.; Kalabukhov, A.; Kuzmin, L.; Claeson, T. THz Josephson properties of grain boundary YBaCuO junctions on symmetric, tilted bicrystal sapphire substrates. *J. Appl. Phys.* **2004**, *96*, 3357. [\[CrossRef\]](#)
17. Kunkel, G.; Bode, M.; Wang, F.; Faley, M.I.; Siegel, M.; Zander, W.; Schubert, J.; Poppe, U.; Braginski, A.I. Comparison of Josephson radiation properties of different YBa₂Cu₃O₇ thin film junctions. *Proc. SPIE Int. Soc. Opt. Eng.* **1994**, *2160*, 33.
18. Batov, I.E.; Jin, X.Y.; Shitov, S.V.; Koval, Y.; Muller, P.; Ustinov, A.V. Detection of 0.5 THz radiation from intrinsic Bi₂Sr₂CaCu₂O₈ Josephson junctions. *Appl. Phys. Lett.* **2006**, *88*, 262504. [\[CrossRef\]](#)
19. An D.Y.; Yuan, Jie, Kinev, N.; Li, M.Y.; Huang, Y.; Ji, M.; Zhang, H.; Sun, Z.L.; Kang, L.; Jin, B.B. Terahertz emission and detection both based on high-Tc superconductors: Towards an integrated receiver. *Appl. Phys. Lett.* **2013**, *102*, 092601. [\[CrossRef\]](#)
20. Tarasov, M.; Stepantsov, E.; Lindstrom, T.; Lohmus, A.; Ivanov, Z. Submillimeter-wave quasioptical integrated tester based on bicrystal Josephson junctions. *Physica C* **2002**, *372–376*, 347. [\[CrossRef\]](#)
21. Ozyuzer, L.; Koshelev, A.E.; Kurter, C.; Gopalsami, N.; Li, Q.; Tachiki, M.; Kadowaki, K.; Yamamoto, T.; Minami, H.; Yamaguchi, H. Emission of coherent THz radiation from superconductors. *Science* **2007**, *318*, 1291. [\[CrossRef\]](#)
22. Kakeya, I.; Omukai, Y.; Yamamoto, T.; Kadowaki, K.; Suzuki, M. Effect of thermal inhomogeneity for terahertz radiation from intrinsic Josephson junction stacks of BSCCO. *Appl. Phys. Lett.* **2012**, *100*, 242603. [\[CrossRef\]](#)
23. Shaikhaidarov, R.; Antonov, V.N.; Casey, A.; Kalaboukhov, A.; Kubatkin, S.; Harada, Y.; Onomitsu, K.; Tzalenchuk, A.; Sobolev, A. Detection of Coherent Terahertz Radiation from a High-Temperature Superconductor Josephson Junction by a Semiconductor Quantum-Dot Detector. *Phys. Rev. Appl.* **2016**, *5*, 024010. [\[CrossRef\]](#)
24. Nagatsuma, T.; Enpuku, K.; Yoshida, K.; Irie, F. Flux-flow-type Josephson oscillator for millimeter and submillimeter wave region. II. Modeling. *J. Appl. Phys.* **1984**, *56*, 3284. [\[CrossRef\]](#)
25. Yoshida, K.; Nagatsuma, T.; Sueoka, K.; Enpuku, K.; Irie, F. Effects of junction geometry on performance of flux-flow type Josephson oscillator. *IEEE Trans. Magn.* **1985**, *21*, 899. [\[CrossRef\]](#)
26. Zhang, Y.M.; Winkler, D.; Claeson, T. Linewidth measurements of Josephson flux-flow oscillators in the band 280–330 GHz. *Appl. Phys. Lett.* **1993**, *62*, 3195. [\[CrossRef\]](#)
27. Koshelets, V.P.; Shchukin, A.; Lapytskaya, I.L.; Mygind, J. Spectral linewidth of autonomous and injection-locked flux-flow oscillators. *Phys. Rev. B* **1995**, *51*, 6536. [\[CrossRef\]](#)
28. Ustinov, A.V.; Kohlstedt, H.; Henne, P. Giant Radiation Linewidth of Multifluxon States in Long Josephson Junctions. *Phys. Rev. Lett.* **1996**, *77*, 3617. [\[CrossRef\]](#)
29. Koshelets, V.P.; Shitov, S.V.; Shchukin, A.V.; Filippenko, L.V.; Mygind, J.; Ustinov, A.V. Self-pumping effects and radiation linewidth of Josephson flux-flow oscillators. *Phys. Rev. B* **1997**, *56*, 5572. [\[CrossRef\]](#)
30. Koshelets, V.P.; Dmitriev, P.N.; Sobolev, A.S.; Pankratov, A.L.; Khodos, V.V.; Vaks, V.L.; Baryshev, A.M.; Wesselius, P.R.; Mygind, J. Line width of Josephson flux flow oscillators. *Physica C* **2002**, *372–376*, 316. [\[CrossRef\]](#)
31. Carapella, G.; Martucciello, N.; Costabile, G. Experimental investigation of flux motion in exponentially shaped Josephson junctions. *Phys. Rev. B* **2002**, *66*, 134531. [\[CrossRef\]](#)
32. Nagatsuma, T.; Enpuku, K.; Sueoka, K.; Yoshida, K.; Irie, F. Flux-flow-type Josephson oscillator for millimeter and submillimeter wave region. III. Oscillation stability. *J. Appl. Phys.* **1985**, *58*, 441. [\[CrossRef\]](#)
33. YZhang, M.; Wu, P.H. Numerical calculation of the height of velocity-matching step of flux-flow type Josephson oscillator. *J. Appl. Phys.* **1990**, *68*, 4703. [\[CrossRef\]](#)

34. Soriano, C.; Costabile, G.; Parmentier, R.D. Coupling of Josephson flux-flow oscillators to an external RC load. *Supercond. Sci. Technol.* **1996**, *9*, 578. [\[CrossRef\]](#)
35. Salerno, M.; Samuelsen, M.R. Phase locking and flux-flow resonances in Josephson oscillators driven by homogeneous microwave fields. *Phys. Rev. B* **1999**, *59*, 14653. [\[CrossRef\]](#)
36. Cirillo, M.; Merlo, V.; Gronbech-Jensen, N. Analysis of linear branches in the IV characteristics of Josephson junctions. *IEEE Trans. Appl. Supercond.* **1999**, *9*, 4139. [\[CrossRef\]](#)
37. Pankratov, A.L. Long Josephson junctions with spatially inhomogeneous driving. *Phys. Rev. B* **2002**, *66*, 134526. [\[CrossRef\]](#)
38. Pankratov, A.L.; Sobolev, A.S.; Koshelets, V.P.; Mygind, J. Influence of surface losses and the self-pumping effect on current-voltage characteristics of a long Josephson junction. *Phys. Rev. B* **2007**, *75*, 184516. [\[CrossRef\]](#)
39. Matrozova, E.A.; Revin, L.S.; Pankratov, A.L. The effect of bias feed profile on the linewidth of noisy Josephson flux flow oscillator. *J. Appl. Phys.* **2012**, *112*, 053905. [\[CrossRef\]](#)
40. Pankratov, A.L. Minimizing the linewidth of the flux-flow oscillator. *Appl. Phys. Lett.* **2008**, *92*, 082504. [\[CrossRef\]](#)
41. Pankratov, A.L. Noise self-pumping in long Josephson junctions. *Phys. Rev. B* **2008**, *78*, 024515. [\[CrossRef\]](#)
42. Gulevich, D.R.; Koshelets, V.P.; Kusmartsev, F.V. Josephson flux-flow oscillator: The microscopic tunneling approach. *Phys. Rev. B* **2017**, *96*, 024515. [\[CrossRef\]](#)
43. Gulevich, D.R.; Koshelets, V.P.; Kusmartsev, F.V. Bridging the terahertz gap for chaotic sources with superconducting junctions. *Phys. Rev. B* **2019**, *99*, 060501. [\[CrossRef\]](#)
44. Gulevich, D.R.; Filippenko, L.V.; Koshelets, V.P. Microscopic Tunneling Model of Nb-AlN-NbN Josephson Flux-Flow Oscillator. *J. Low Temp. Phys.* **2019**, *194*, 312. [\[CrossRef\]](#)
45. Winkler, D.; Zhang, Y.M.; Nilsson, P.A.; Stepanov, E.A.; Claeson, T. Electromagnetic properties at the grain boundary interface of a YBa₂Cu₃O₇ bicrystal Josephson junction. *Phys. Rev. Lett.* **1994**, *72*, 1260. [\[CrossRef\]](#) [\[PubMed\]](#)
46. Zhang, Y.M.; Winkler, D.; Nilsson, P.-A.; Claeson, T. Josephson flux-flow resonances in overdamped long YBa₂Cu₃O₇ grain-boundary junctions. *Phys. Rev. B* **1995**, *51*, 8684. [\[CrossRef\]](#)
47. Sung, H.H.; Yang, S.Y.; Horng, H.E.; Yang, H.C. Flux motion in YBCO biepitaxial Josephson junctions. *IEEE Trans. Appl. Supercond.* **1999**, *9*, 3937. [\[CrossRef\]](#)
48. Lombardi, F.; di Uccio, U.S.; Ivanov, Z.; Claeson, T.; Cirillo, M. Flux flow in YBCO grain-boundary Josephson junctions with a four-terminal configuration. *Appl. Phys. Lett.* **2000**, *76*, 2591. [\[CrossRef\]](#)
49. Kuzmin, L.S.; Sobolev, A.S.; Beiranvand, B. Wideband Double-Polarized Array of Cold-Electron Bolometers for OLIMPO Balloon Telescope. *IEEE Trans. Anten. Prop.* **2020**, *68*, in press. [\[CrossRef\]](#)
50. Revin, L.S.; Chiginev, A.V.; Pankratov, A.L.; Masterov, D.V.; Parafin, A.E.; Luchinin, G.A.; Matrozova, E.A.; Kuzmin, L.S. The effect of bias current asymmetry on the flux-flow steps in the grain boundary YBaCuO long Josephson junctions. *J. Appl. Phys.* **2013**, *114*, 243903. [\[CrossRef\]](#)
51. Revin, L.S.; Pankratov, A.L.; Chiginev, A.V.; Masterov, D.V.; Parafin, A.E.; Pavlov, S.A. Asymmetry of the velocity-matching steps in YBCO long Josephson junctions. *Supercond. Sci. Technol.* **2018**, *31*, 045002. [\[CrossRef\]](#)
52. Revin, L.S.; Pankratov, A.L.; Masterov, D.V.; Parafin, A.E.; Pavlov, S.A.; Chiginev, A.V.; Skorokhodov, E.V. Features of Long YBCO Josephson Junctions Fabricated by Preliminary Topology Mask. *IEEE Trans. Appl. Supercond.* **2018**, *28*, 1100505. [\[CrossRef\]](#)
53. Pankratov, A.L.; Pankratova, E.V.; Shamporov, V.A.; Shitov, S.V. Oscillations in Josephson transmission line stimulated by load in the presence of noise. *Appl. Phys. Lett.* **2017**, *110*, 112601. [\[CrossRef\]](#)
54. Tafuri, F.; Kirtley, J.R. Weak links in high critical temperature superconductors. *Rep. Prog. Phys.* **2005**, *68*, 2573. [\[CrossRef\]](#)

Publisher's Note: MDPI stays neutral with regard to jurisdictional claims in published maps and institutional affiliations.



© 2020 by the authors. Licensee MDPI, Basel, Switzerland. This article is an open access article distributed under the terms and conditions of the Creative Commons Attribution (CC BY) license (<http://creativecommons.org/licenses/by/4.0/>).